Journal of the Taiwan Institute of Chemical Engineers xxx (xxxx) xxx

Contents lists available at ScienceDirect

Journal of the Taiwan Institute of Chemical Engineers

journal homepage: www.journals.elsevier.com/journal-of-the-taiwan-institute-of-chemical-engineers

# Mixed-ligand strategies to synthesize Zr-based MOFs for enhanced rhodamine B adsorption

Duo-Syuan Lin [a], Jun-Han Lin [b], To-Yu Wang [a], Ming-Wei Chen [a], Li-Heng Kao [b], Wei-Yu Chen [c], Kanit Manatura [d], Hongta Yang [e], Van-Huy Nguyen [f], Chao-Wei Huang [a,*]

[a] Department of Engineering Science, National Cheng Kung University, Tainan 70101, Taiwan
[b] Department of Chemical and Materials Engineering, National Kaohsiung University of Science and Technology, Kaohsiung 80778, Taiwan
[c] Department of Materials Engineering, National Pingtung University of Science and Technology, Pingtung 912301, Taiwan
[d] Department of Mechanical Engineering, Faculty of Engineering at Kamphaeng Saen Kasetsart University, Kamphaeng Saen campus, Nakhon Pathom 73140, Thailand
[e] Department of Chemical Engineering, National Chung Hsing University, Taichung 402204, Taiwan
[f] Centre for Herbal Pharmacology and Environmental Sustainability, Chettinad Hospital, and Research Institute, Chettinad Academy of Research and Education, Kelambakkam 603103, Tamil Nadu, India

ARTICLE INFO

*Keywords:*
Metal-organic frameworks
Zr-based
Adsorption
Rhodamine B dye
Pseudo-second-order model

ABSTRACT

*Background:* Zirconium-based metal-organic frameworks (Zr-MOFs) are promising adsorbents due to their tunable porosity and structural flexibility. This study explores mix-ligand strategies as a means to introduce structural defects and enhance adsorption performance for pollutant removal.
*Methods:* UiO-66-$NH_2$ served as the parent MOF. Three 10 mol % mixed-ligand strategies—isostructural mixed linkers (IML), heterostructural mixed linkers (HML), and truncated mixed linkers (TML)—were applied using terephthalic acid, isophthalic acid, trimesic acid, and benzoic acid. The samples were performed at 10 mol % using a solvothermal method. Comprehensive characterization was conducted via a solvothermal method and characterized using XRD, FTIR, and BET surface analysis. Adsorption performance was evaluated through rhodamine B (RhB) removal and kinetic modeling.
*Significant Findings:* Among the tested MOFs, IP-10 (isophthalic acid-substituted) achieved the highest BET surface area (1331.87 $m^2/g$) and RhB adsorption capacity $q_e = 24.29$ mg/g. Enhanced adsorption was attributed to optimized pore structures and hydrogen bond-assisted interactions. Kinetic analysis conformed to a pseudo-second-order model, indicating chemisorption as the dominant mechanism. IP-10 also revealed the highest intraparticle diffusion coefficient (2.8133 $mg \cdot g^{-1} \cdot min^{-1}$), confirming efficient pore utilization. These findings demonstrate the potential of tailored mixed-ligand Zr-MOFs for advanced dye adsorption applications.

## 1. Introduction

The textile industry, a cornerstone of modern life, is also a major source of environmental pollution due to its extensive use of synthetic dyes [1]. Over 35 % of dyes are discharged into ecosystems during processing [2]. Among these dyes, rhodamine B (RhB) is particularly harmful, with toxic, bioaccumulative, and potentially transgenerational effects on aquatic and terrestrial organisms [3,4]. Its widespread presence in textile wastewater highlights the need for efficient dye removal technologies [5]. Conventional treatment methods such as photocatalysis [6], membrane filtration [7], biodegradation [8], and adsorption [9] have been employed. Among them, adsorption is especially attractive due to its simplicity, cost-effectiveness, and minimal secondary pollution. Research efforts have thus focused on developing high-performance adsorbents for dye removal [10–12]. Metal-organic frameworks (MOFs) have recently emerged as promising adsorbent materials. Comprising metal centers and organic linkers, MOFs offer high surface areas, tunable pore sizes, and modifiable surface chemistry. These features make them versatile for applications such as gas separation [13], drug delivery [14], catalysis [15], photocatalysis [16,17], and particularly, dye adsorption [18]. The ability to tailor MOF structures at the molecular level further enhances their potential for targeted

* Corresponding author.
*E-mail addresses:* n98121088@gs.ncku.edu.tw (D.-S. Lin), f109146150@nkust.edu.tw (J.-H. Lin), n98121070@gs.ncku.edu.tw (T.-Y. Wang), n96134530@gs.ncku.edu.tw (M.-W. Chen), biny@nkust.edu.tw (L.-H. Kao), wychen@mail.npust.edu.tw (W.-Y. Chen), hyang@dragon.nchu.edu.tw (H. Yang), huangcw@gs.ncku.edu.tw (C.-W. Huang).

https://doi.org/10.1016/j.jtice.2025.106246
Received 11 December 2024; Received in revised form 5 June 2025; Accepted 15 June 2025

wastewater treatment [19,20].

Recent studies have investigated a range of MOFs and their composites for the adsorption of RhB, as summarized in Table S1. For example, Fe-based MOFs synthesized by Ren et al. demonstrated a maximum adsorption capacity of 136 mg/g at pH 6 [21], while Cui et al.'s ZnO/Zr-MOF(bpy) composite achieved 98.2 mg/g at 10 ppm initial RhB concentration [22]. Similarly, Ibrahim et al. reported 97.5 mg/g adsorption using 25 wt % PMA-Sr-MOF [23], and Patil et al. obtained 66.67 mg/g with a Ce/Zr-based MOF hybrid at 30 ppm [24]. Given their use in aqueous environments, the development of water-stable MOFs—particularly those based on zirconium (Zr)—has attracted considerable attention [25]. Zr-MOFs not only exhibit high thermal stability [26,27] but also retain structural integrity in acidic solutions and organic solvents [28,29]. This resilience is attributed to the strong Zr-carboxylate bonds and high connectivity of the Zr clusters, making them suitable for practical applications [30]. For instance, UiO-66 and related Zr-MOFs have shown remarkable stability under harsh chemical conditions, as highlighted by Kandiah et al. [31]. Furthermore, Kim et al. compared dye adsorption behaviors across water-stable MOFs, including UiO-66, UiO-67, and MIL-100(Fe), and found that Zr-MOFs exhibited stronger dye-framework interactions based on FTIR spectral shifts, likely due to the involvement of Zr–O clusters. In contrast, MIL-100(Fe) showed minimal changes post-adsorption, indicating weaker dye binding [32]. Given their superior stability and interaction with dye molecules, Zr-based MOFs were selected as the focus of this study.

Defect engineering has emerged as a powerful strategy for enhancing the performance of MOFs. In particular, introducing structural defects can improve adsorption capacity without compromising the material's stability in aqueous environments. Recent studies have shown that Zr-MOFs can accommodate high concentrations of defects while maintaining excellent chemical and thermal stability [33]. However, defects in MOFs have complex effects on porosity, mechanical strength, and surface acidity (both Lewis and Brønsted), all of which influence adsorption behavior [34]. Two primary types of defects are typically observed in Zr-MOFs: missing linker and missing cluster defects [35]. The former occurs when organic linkers are absent, creating coordination vacancies at nearby Zr sites [36], while the latter involves the loss of Zr-O clusters along with their linkers, disrupting the surrounding framework [37]. Such defects can be intentionally introduced and tuned through synthesis conditions. For instance, Jiang et al. demonstrated that functionalized ligands could replace formate-terminated $Zr_6$ clusters in MOF-808, enabling post-synthetic modification with target groups [38]. Similarly, Ou et al. employed acetic acid as a modulator to generate missing linker defects in UiO-66, which increased the number of unsaturated Zr sites and significantly enhanced toluene adsorption [39].

On the other hand, elevated linker concentrations promote stronger coordination with secondary building units (SBUs), leading to more nucleation sites and, consequently, smaller crystal sizes [40]. For instance, Wu et al. demonstrated that adjusting acetic acid concentration and synthesis time in UiO-66 enabled controlled formation of missing linker defects, yielding materials with pore volumes up to 1.0 $cm^3/g$ and BET surface areas as high as 1600 $m^2/g$, well above the theoretical values of defect-free UiO-66 by 150 % and 60 %, respectively [36]. Behrens et al. systematically investigated various modulators, including acetic, benzoic, and trifluoroacetic acids, in the synthesis of UiO-66 and UiO-67, revealing their impact on crystal morphology and structural integrity [41]. Similarly, Ren et al. showed that incorporating formic acid during MOF-808 synthesis significantly improved crystallinity, producing well-defined octahedral crystals and reducing particle agglomeration in a dose-dependent manner [42]. It highlights the critical role of modulation strategies in controlling both crystal architecture and defect density for optimizing the performance of MOFs in adsorption applications.

Recent efforts have focused on tuning the structural and functional properties of MOFs through mixed-ligand strategies, which allow modulation of pore size, framework functionality, and defect density [43]. Three primary approaches are commonly employed: (1) isostructural mixed linker (IML) systems, which incorporate chemically similar linkers of comparable size into a uniform framework [44]; (2) heterostructural mixed linker (HML) systems, which combine linkers with distinct coordination geometries to introduce functional diversity and enlarge pore architecture [45]; and (3) truncated mixed linker (TML) strategies, in which monomers with fewer reactive groups are co-assembled to control crystal morphology and surface properties [46]. The spatial distribution of truncated linkers depends on the relative rates of bond formation and exchange: rapid growth leads to their integration near defect sites, while faster exchange favors surface localization, influencing particle size and shape [47]. Despite growing interest, few studies have systematically explored the impact of mixed-linker strategies on the adsorption performance of Zr-based MOFs [48–50]. Leveraging the inherent defect tolerance and aqueous stability of Zr-MOFs, our study investigates the influence of different organic linker substitutions using XRD, FTIR, and BET analyses to identify optimal compositions. A series of mixed-ligand Zr-MOFs were synthesized using IML, HML, and TML approaches to enhance dye adsorption capacity through defect engineering. Furthermore, adsorption kinetics models were applied to evaluate the adsorption behavior of the resulting materials.

## 2. Experimental

### 2.1. Chemicals

Zirconium(IV) tetrachloride ($ZrCl_4$, CAS: 10,026–11–6, 98.0 %), terephthalic acid ($H_2BDC$, CAS: 100–21–0, 99.0 %), benzoic acid (BA, CAS: 65–85–0, 99.6 %), and rhodamine B (RhB, CAS: 81–88–9, 98.0 %) were obtained from Acros Organics. 2-aminoterephthalic acid ($NH_2$-BDC, CAS: 10,312–55–7, 99.0 %), trimesic acid ($H_3BTC$, CAS: 554–95–0, 98.0 %), and isophthalic acid (IP, CAS: 121–91–5, 99.0 %) were supplied by Alfa Aesar. Dimethylformamide (DMF, CAS: 68–12–2, 99.5 %) and formic acid (FA, CAS: 64–18–6, 98–100 %) were procured from Fisher Chemical. Ethanol (EtOH, CAS: 64–17–5, 95.0 %) was provided by J.T. Baker.

### 2.2. Synthesis

#### 2.2.1. Synthesis of UiO-66-$NH_2$ and MOF-808

The synthesis of UiO-66-$NH_2$ was conducted using a solvothermal method. Initially, a mixed solution was prepared by combining 30 mL of DMF and 15 mL of FA. DMF acted as the primary solvent, while FA served as a modulating agent to assist in crystal coordination and growth [20,51]. The solution was stirred for 5 min to ensure thorough mixing before adding 0.9050 g of $NH_2$-BDC as the organic linker. After stirring for 10 mins, 1.1650 g of $ZrCl_4$ was introduced as the metal node precursor. The mixture was further stirred for 3 min, followed by the slow addition of 3 mL of deionized (DI) water to facilitate the hydrolysis of $ZrCl_4$ for a more homogeneous reaction. The total stirring time was 30 min, after which the mixture was subjected to ultrasonic treatment for another 30 min. The resulting mixture was then delivered to a 50 mL Teflon-lined autoclave and maintained at 100 °C for 48 h. After cooling to room temperature, the liquid was separated by centrifugation and filtered. The solid product was washed with EtOH by stirring for 10 min, followed by vacuum filtration. This washing process was repeated three times, and the product was washed once with acetone and filtered. The solid was then dried at 100 °C for one day. The final product, UiO-66-$NH_2$, was obtained by grinding the dried material.

The synthesis of MOF-808 followed a similar procedure. A mixed solution of 30 mL DMF and 30 mL FA was prepared and stirred until homogeneously mixed. Then, 1.0507 g of $H_3BTC$ was added as the organic linker, and the solution was stirred for 10 min before the

addition of $ZrCl_4$. The subsequent steps were identical to those used in the synthesis of UiO-66-$NH_2$. The final product obtained through this process was designated as MOF-808.

*2.2.2. Synthesis of mixed-MOFs with different substitution ratios*

To study the impact of different substitution ratios on the structure and properties of mixed-MOFs, the effect of substituting the original ligand ($NH_2$-BDC) in UiO-66-$NH_2$ with varying amounts of $H_3BTC$ was examined. Among the chosen linkers, the significant structural differences between $H_3BTC$ and $NH_2$-BDC may influence the framework's stability or structural integrity. Therefore, $H_3BTC$ was selected to explore the effects of substitution ratios in mixed-MOFs. The substitution ratios were 10, 20, 30, 40, and 50 mol % of $H_3BTC$, replacing the $NH_2$-BDC ligand in UiO-66-$NH_2$. These specific ratios were selected to balance the potential for $H_3BTC$ to disrupt the overall framework structure if used excessively, against the inability to effectively engineer defects if the substitution is too minimal. Therefore, the chosen substitution ratios provide a range for studying their effects on the resulting MOFs.

The synthesis began by preparing a mixed solution of 30 mL DMF as the main solvent and 15 mL FA as a modulator. This solution was stirred for 5 min before adding 0.9050 g of $NH_2$-BDC. After 10 min of stirring, $H_3BTC$ was added according to the desired molar ratios ($NH_2$-BDC: $H_3BTC$ = 9:1, 8:2, 7:3, 6:4, 5:5). The mixture was further stirred for 10 min before introducing 1.1650 g of $ZrCl_4$. The remaining steps followed the same procedure as the synthesis of UiO-66-$NH_2$. The products synthesized with different $H_3BTC$ substitution ratios were designated as BTC-10, BTC-20, BTC-30, BTC-40, and BTC-50, corresponding to 10 %, 20 %, 30 %, 40 %, and 50 % molar ratios of $H_3BTC$, respectively.

*2.2.3. Synthesis of mixed-MOFs with different organic linker substitutions*

This section explores the effects of different organic linker substitutions on the design of defect engineering strategies in mixed-MOFs for the adsorption to remove pollutants. Various strategies were employed to create mixed-ligand MOFs with different linker substitutions, as shown in Fig. 1. For the IML strategy, $H_2BDC$ was used to prepare mixed-ligand MOFs. For the HML strategy, two different linkers, $H_3BTC$ and IP, were individually utilized to synthesize mixed-ligand MOFs. Then, BA was employed to produce mixed-ligand MOFs following the TML strategy.

The synthesis began with the preparation of a mixed solution of 30 mL DMF and 15 mL FA. The mixture was stirred for 10 mins after adding 0.9050 g of $NH_2$-BDC. Depending on the specific mixed-MOFs to be synthesized, $H_3BTC$, $H_2BDC$, IP, or BA were added at a molar ratio of 1:9 relative to $NH_2$-BDC. Following an additional 10 mins of stirring, 1.1650 g of $ZrCl_4$ was introduced. The remaining steps were conducted according to the established UiO-66-$NH_2$ synthesis protocol. The resulting products were named according to their respective organic linker substitutions: BTC-10, BDC-10, IP-10, and BA-10, representing the use of $H_3BTC$, $H_2BDC$, IP, and BA, respectively.

## 2.3. Characterization

The synthesized MOFs were characterized via various analytical techniques to determine their structural, morphological, and surface properties. X-ray diffraction (XRD) patterns were obtained using a BRUKER D8 Advance diffractometer. The scanning rate was 2°/min, with a scanning range of $2\theta = 5°$ to 45°. The data was compared against the Joint Committee on Powder Diffraction Standards (JCPDS) card numbers to confirm the crystalline structure of the synthesized adsorbents. Fourier-transform infrared spectroscopy (FTIR) spectra were collected using a Perkin Elmer Spectrum One FT-IR Spectrometer. This technique identifies molecular structures and bonding conditions based on the characteristic absorption of infrared wavelengths by the sample molecules. Before analysis, samples were dried in an oven at 105 °C to eliminate moisture interference. The scanning range was set from 600 to 4000 $cm^{-1}$. Specific surface areas, porosity, and the Brunauer-Emmett-Teller (BET) surface were evaluated using an ASAP 2020 PLUS instrument. A JSM-6710F scanning electron microscope (SEM) was utilized to analyze the surface morphology of the prepared MOFs. The zeta potential of the MOFs was measured using a Malvern Zetasizer Nano ZS90 to evaluate their surface charge properties. For the characterization of

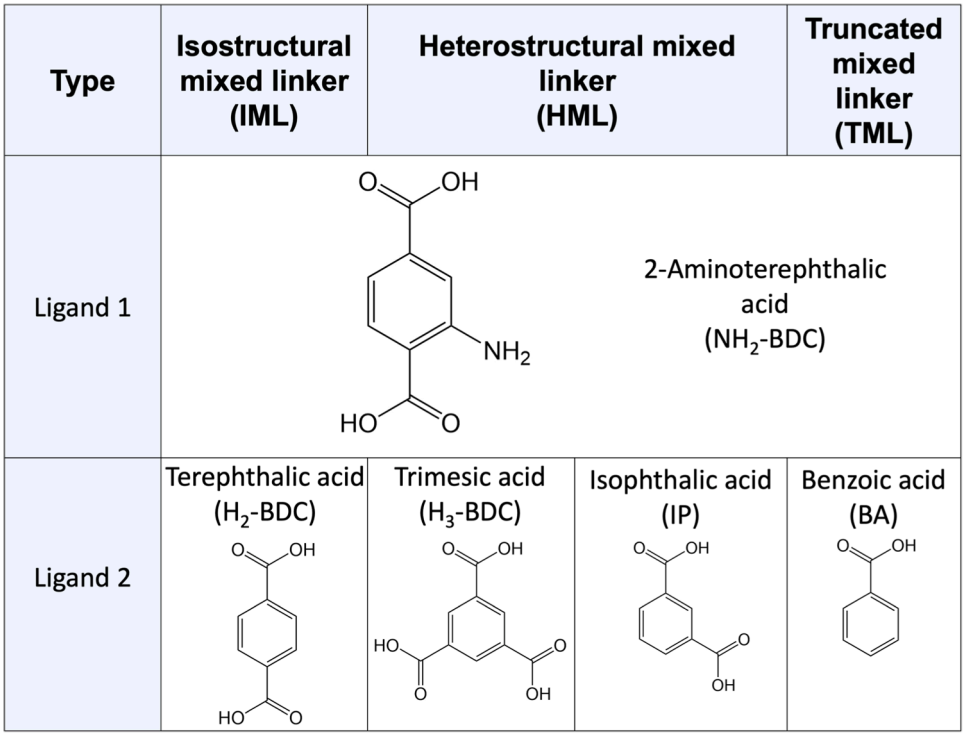


**Fig. 1.** Overview of the synthetic planning for IML, HML, and TML strategies.

mixed-ligand MOFs, $^1$H NMR spectra were recorded on a Bruker AVANCE III HD 600 MHz NMR Spectrometer to confirm the incorporation of the different ligands.

### 2.4. Adsorption test and kinetic analysis

#### 2.4.1. Adsorption test

Following literature precedent [22,52], RhB adsorption tests were conducted using a 150 mL aqueous dye solution at an initial concentration of 10 ppm. RhB was dissolved in deionized water. A total of 50 mg of MOF powder was added, and the mixture was shielded from light using aluminum foil. To capture the rapid initial adsorption phase, 4 mL aliquots were collected every 2 min during the first 10 min. Additional samples were taken at 15, 20, 25, 30, 40, 50, and 60 min. Each sample was centrifuged at 15,000 rpm for 10 min, and the resulting supernatant was transferred to 15 mL tubes for analysis. RhB concentrations were determined using a Shimadzu UV-1800 spectrophotometer. Concentrations were calculated using a calibration curve based on RhB's characteristic absorption peak at the wavelength of 554 nm.

#### 2.4.2. Adsorption kinetic analysis

Adsorption kinetics can be explained using two types of models to analyze the removal of pollutants from aqueous solutions. First, kinetic models, including pseudo-first-order, pseudo-second-order, and Langmuir kinetic models, explain the interactions between pollutant molecules and adsorbent surfaces, without considering diffusion effects [53]. Second, diffusion models include membrane-pore diffusion, membrane-surface diffusion, and membrane-parallel pore and surface diffusion models. These models assume that interactions between pollutants and active sites occur instantaneously relative to the diffusion steps, thus making diffusion steps the rate-controlling factors [54]. Understanding adsorption kinetics is essential for evaluating the performance of adsorbents and elucidating potential mechanisms. The adsorption process using solid adsorbents for liquid dyes typically involves two consecutive steps: (1) solute migration from bulk solution to the liquid layer surrounding the adsorbent particles, and (2) solute diffusion through the layer until it reaches the adsorption surface (membrane diffusion). Typically, the first step occurs rapidly, making the second step the rate-determining step. Nevertheless, in porous adsorbents, intraparticle diffusion, particularly solute diffusion into the internal surface of the adsorbent, can also be the rate-determining step [55].

The equilibrium adsorption amount ($q_e$, mg/g) and removal efficiency (R, %) of the adsorbent for the adsorbate are calculated using Eqs. (1) and (2) [56]:

$$q_e = (C_0 - C_e) \times \frac{V}{M} \tag{1}$$

$$R = \frac{(C_0 - C_e)}{C_0} \times 100\% \tag{2}$$

where $C_0$ was the initial concentration of the adsorbate (mg/L), $C_e$ was the equilibrium concentration of the adsorbate (mg/L), $V$ was the volume of the solution (L), and $M$ was the mass of the adsorbent (g).

For the pseudo-first-order kinetic model, the reaction rate is proportional to the concentration of a single reactant and is primarily used for adsorption in liquid phases [57,58]. The calculation is given by Eq. (3):

$$\ln (q_e - q_t) = -k_1 t + \ln (q_e) \tag{3}$$

This can also be rearranged into Eq. (4):

$$-\ln \left( \frac{q_e - q_t}{q_e} \right) = k_1 t \tag{4}$$

where $q_e$ was the equilibrium adsorption amount of the adsorbate (mg/g), $q_t$ was the adsorption amount of the adsorbate at time (mg/g), $k_1$ was the pseudo-first-order kinetic rate constant (min$^{-1}$), and $t$ was time (min).

The pseudo-second-order kinetic model assumes that the reaction rate is linearly related to the concentrations of two reactants. This model suggests that the adsorption is controlled by chemical interactions such as valency, coordination, ion exchange, and chelation [59]. The equation for this model is given by Eq. (5), and the slope and intercept of the plot of $\frac{t}{q_t}$ versus $t$ can be used to calculate the rate constant ($k_2$) and the equilibrium adsorption capacity ($q_e$):

$$\frac{t}{q_t} = \frac{1}{k_2 q_e^2} + \frac{t}{q_e} \tag{5}$$

where $q_e$ was the equilibrium adsorption capacity (mg/g), $q_t$ was the adsorption capacity at time t (mg/g), $k_2$ was the pseudo-second-order kinetic rate constant (g·mg$^{-1}$·min$^{-1}$), and t was time (min).

If a plot of the adsorption of pollutant ions versus the square root of time produces a straight line, it suggests that intraparticle diffusion is the rate-determining step in the adsorption process. The intraparticle diffusion equation, first proposed by Weber and Morris [60], is expressed as Eq. (6):

$$q_t = k_i t^{0.5} + C \tag{6}$$

where $q_t$ was adsorption capacity at time (mg/g), $k_i$ was intraparticle diffusion rate constant (g·mg$^{-1}$·min$^{-1}$), t was time (min), and C was boundary layer effect constant.

A larger intercept $C$ indicates a larger role of surface adsorption in the rate-determining step. If the plot of $q_t$ versus $t^{0.5}$ does pass through the origin, it suggests that intraparticle diffusion is not the sole rate-determining step. Due to mass transfer effects, the plot of $q_t$ against $t^{0.5}$ initially shows a curve during a small initial time frame, followed by a linear segment and a plateau. The initial curve is ascribed to external diffusion, while the linear segment is due to intraparticle diffusion [40].

## 3. Results and discussion

### 3.1. Effects of different substitution ratios on mixed-MOFs

Fig. 2(a) illustrates the XRD patterns of the synthesized UiO-66-NH$_2$, MOF-808, and the mixed-MOFs formed by substituting 10 mol % - 50 mol % of H$_3$BTC for NH$_2$-BDC in UiO-66-NH$_2$. First, the XRD pattern of the prepared UiO-66-NH$_2$ was compared with the simulated pattern from the database [61]. Characteristic diffraction peaks were observed at 7.36°, 8.48°, 12.04°, 14.15°, 17.08°, 22.08°, and 25.68°, corresponding to the (111), (002), (022), (113), (004), and (224) crystal planes of the UiO-66 structure, respectively. The addition of formic acid as a modulator altered the ligand environment, which was beneficial for the formation and growth of the crystals, thus improving the crystallinity [39]. Additionally, the XRD pattern of the prepared MOF-808 was compared with the simulated pattern from the literature [62]. The characteristic peaks at 8.7°, 10°, and 10.9° were closely aligned with the simulated pattern, corresponding to the (222), (400), and (331) crystal planes, indicating the successful synthesis of MOF-808 [63].

Fig. 2(b) shows the XRD patterns of mixed-MOFs with the substitution ratios from 10 mol % to 40 mol %. Their diffraction peaks at 7.36°, 8.48°, 12.04°, 14.15°, 17.08°, 22.08°, and 25.68° correspond to the characteristic peaks of the UiO-66 crystal planes, indicating that the core structure of UiO-66 is retained up to a 40 mol % substitution of H$_3$BTC. However, when the substitution ratio was increased to 50 mol %, the characteristic peaks became more aligned with those of MOF-808, suggesting that the high substitution level of H$_3$BTC led to stronger competitive coordination with NH$_2$-BDC. This competitive coordination likely disrupted the original UiO-66-NH$_2$ structure, resulting in a structural transformation toward MOF-808.

Fig. 2(c) presents the FTIR spectra of the synthesized mixed-MOFs,

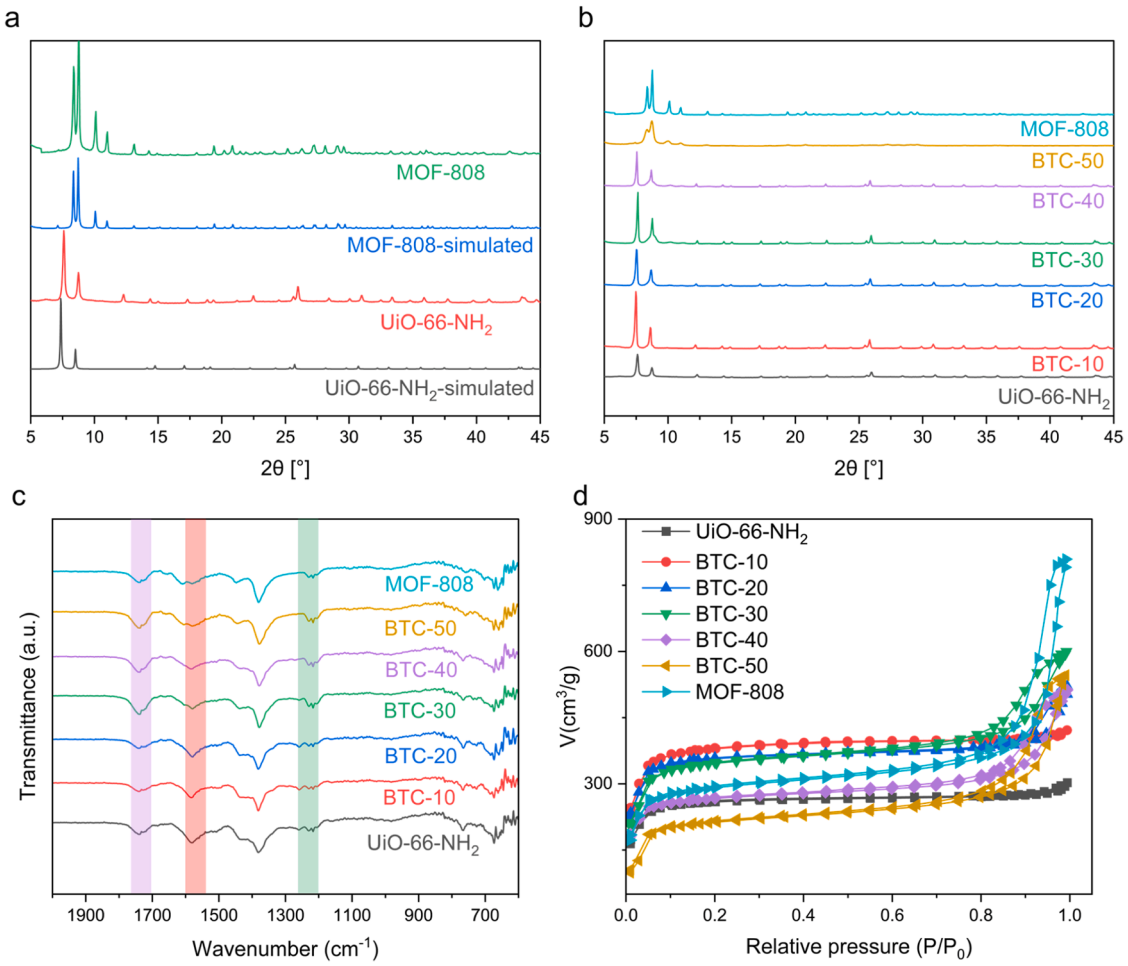


**Fig. 2.** (a) XRD patterns of synthesized MOF-808 and UiO-66-$NH_2$ with literature simulations; (b) XRD patterns, (c) FTIR results, (d) $N_2$ isothermal adsorption-desorption results of the synthesized MOF-808, UiO-66-$NH_2$, and the mixed-MOFs with different $H_3BTC$ substitution ratios (BTC-10, BTC-20, BTC-30, BTC-40, and BTC-50).

illustrating key functional group vibrations. A distinct peak at 1760 $cm^{-1}$ corresponds to the $C = O$ stretching vibration from carboxylic acid groups [64], as highlighted by the light blue shaded area in Fig. 2(b). Additionally, a peak within the 1210–1163 $cm^{-1}$ range, associated with C—O stretching of the carboxylic acid group, is observed [64], indicated by the gray shaded area. The spectra also show a peak in the 1650–1580 $cm^{-1}$ region, attributed to the N—H bending vibration from $NH_2$-BDC [64], highlighted by the red-shaded area. Another characteristic peak is found between 1385–138 $cm^{-1}$, corresponding to C—H bending [64], and a C—H bending peak is present in the 735–775 $cm^{-1}$ range [65]. The overall FT-IR spectra of the mixed-MOFs, which were substituted with $H_3BTC$, exhibit no significant differences compared to UIO-66-$NH_2$, as evidenced by the similarity between the spectra of the other samples and UiO-66-$NH_2$ [66]. Notably, the intensity of the N—H bending peak at 1650–1580 $cm^{-1}$ gradually decreases as the substitution ratio increases due to the replacement of $NH_2$-BDC by $H_3BTC$, which lacks the N—H functional group. This observation provides indirect evidence for the successful synthesis of mixed-ligand MOFs, as the progressive weakening of the N—H peak with increasing $H_3BTC$ substitution confirms the structural modification of the MOFs.

Fig. 2(d) illustrates the nitrogen adsorption-desorption isotherms for mixed-MOFs with varying $H_3BTC$ substitution ratios and for MOF-808. The isotherms of these materials exhibit characteristics of type IV adsorption curves, indicative of the presence of both microporous and mesoporous structures [55]. In contrast, the UiO-66-$NH_2$ sample displays a type I adsorption curve, which is typical of a purely microporous structure. The BET surface area data, summarized in Table 1, reveal that as the substitution ratio of $H_3BTC$ increases, the surface area initially increases and then decreases. This trend is likely due to competitive coordination between $H_3BTC$ and $NH_2$-BDC for metal ions, which affects the overall framework structure, consistent with previous literature [36]. The pore structure of UiO-66-$NH_2$ and BTC-10 primarily falls within the microporous scale. However, the isotherms for BTC-20, BTC-30, and BTC-40 show a noticeable hysteresis loop, indicating the presence of both mesoporous and microporous structures. Moreover, BTC-50 and MOF-808 both exhibit similar hysteresis behavior, confirming the existence of both micropores and mesopores. Notably, the pore sizes of BTC-50 and MOF-808 exceed 5 nm, the largest observed among the synthesized materials. This can be attributed to the

**Table 1**
BET results of synthesized MOF-808, UiO-66-$NH_2$, and the mixed-MOFs with different $H_3BTC$ substitution ratios (BTC-10, BTC-20, BTC-30, BTC-40, and BTC-50).

| Adsorbent | Surface area ($m^2$/g) | Pore Volume ($cm^3$/g) | Pore diameter (nm) |
|---|---|---|---|
| UiO-66-$NH_2$ | 791.47 | 0.33 | 2.37 |
| BTC-10 | 1161.65 | 0.45 | 2.24 |
| BTC-20 | 1089.45 | 0.44 | 2.96 |
| BTC-30 | 1078.15 | 0.39 | 3.47 |
| BTC-40 | 819.80 | 0.32 | 3.87 |
| BTC-50 | 668.13 | 0.30 | 5.05 |
| MOF-808 | 909.13 | 0.30 | 5.50 |

inherently larger pore size of MOF-808 compared to UiO-66-NH₂. Additionally, the XRD results demonstrate that the crystal phase of BTC-50 closely resembles that of MOF-808, further corroborating the consistency between pore size and crystal structure observations.

Preliminary RhB adsorption tests were also conducted to evaluate the performance of mixed-ligand MOFs with varying $H_3BTC$ substitution ratios, as shown in Fig. S1. The results showed comparable adsorption capacities across the different substitution levels. Among them, BTC-10 demonstrated the highest crystallinity based on XRD analysis and the largest specific surface area according to BET measurements. Given these favorable properties, BTC-10 was selected as the optimal composition for further study. Accordingly, a fixed substitution ratio of 10 mol % was applied in subsequent experiments to explore the effects of different organic ligands on pollutant adsorption performance.

### 3.2. Different organic ligand substitutions in mixed-MOFs

#### 3.2.1. XRD results

To assess whether the substitution of different organic ligands alters the structure of the initial MOF and to confirm the successful synthesis of mixed-MOFs, XRD analysis was carried out, as shown in Fig. 3(a). The XRD patterns reveal distinct diffraction peaks at 7.36°, 8.48°, 12.04°, 14.15°, 17.08°, 22.08°, and 25.68°, which correspond to the (111), (002), (022), (113), (004), and (224) crystal planes of UiO-66-NH₂, respectively. These results indicate that the initial UiO-66-NH₂ structure is retained across all samples. The enhanced crystallinity observed in BTC-10 is attributed to the favorable coordination environment provided by formic acid in the solvent, which promotes better crystal formation [66]. However, for the other substituted samples, a noticeable decrease in the intensity of the characteristic peak at $2\theta = 25.68°$, corresponding to the (224) plane of UiO-66-NH₂, was observed. This reduction in peak intensity suggests the introduction of structural defects due to ligand substitution. Specifically, the BA-10 sample, with its TML design, exhibited the weakest peak intensity, indicating a higher level of defects in the structure. The BDC-10 sample, designed with an IML strategy, maintained a more intact framework, but still showed reduced peak intensity due to the influence of defects. The IP-10 sample, which involved HML substitution, likely introduced more significant structural defects, leading to a further reduction in peak intensity. These XRD results suggest that while the core UiO-66-NH₂ structure is generally preserved, the extent of structural disruption and defect formation varies depending on the specific organic ligand substitution strategy employed.

The spectra of the mixed-MOFs generally exhibit similar features to those of UiO-66-NH₂. As shown in Fig. 3(b), a characteristic $C = O$ stretching peak from carboxylic acid groups is observed at 1760 $cm^{-1}$ (highlighted by the light blue shaded area) [67]. Additionally, a distinct N—H bending peak from NH₂-BDC appears between 1650–1580 $cm^{-1}$ (highlighted by the red shaded area), while a C—H bending peak is observed in the 1385–1380 $cm^{-1}$ range [68]. However, it is noteworthy that the $C = O$ stretching peak at 1760 $cm^{-1}$ is significantly reduced or even absent in some of the substituted mixed-MOFs. This attenuation or

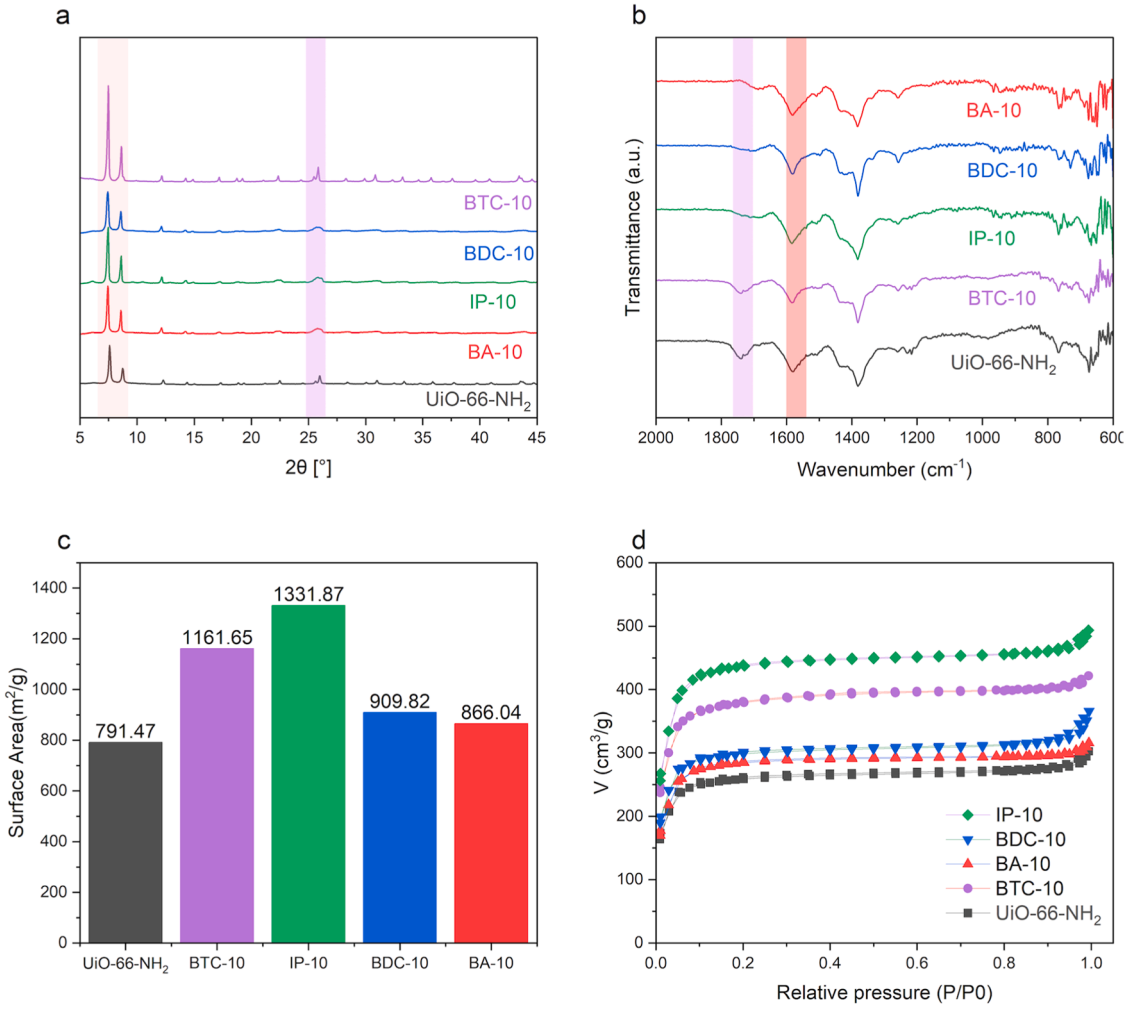


**Fig. 3.** (a) XRD patterns, (b) FTIR results, (c) BET surface area, and (d) $N_2$ isothermal adsorption-desorption results of the synthesized UiO-66-NH₂ with the 10 mol % substitutions of different organic ligands, including BTC-10, BDC-10, IP-10, BA-10, and the pristine.

disappearance of the $C = O$ peak is ascribed to the absence of free carboxylic groups in the structures of BA and BDC, which were used as substituents. Furthermore, the coordination of these ligands with metal nodes leads to the loss of the $C = O$ bond, explaining the observed reduction in the $C = O$ stretching peak.

As presented in Fig. 3(c), the BET analysis reveals that all substituted mixed-MOFs exhibited higher specific surface areas compared to the initial UiO-66-$NH_2$. Notably, the IP-10 sample achieved the highest specific surface area of 1331.87 $m^2/g$, approximately 1.7 times greater than the original UiO-66-$NH_2$, which had a surface area of 791.47 $m^2/g$. This increase in surface area can be attributed to the fact that IP-10 is less prone to aggregation compared to the other mixed-MOFs, resulting in better dispersion and more exposed pores. This observation is further supported by SEM characterization. The isothermal adsorption-desorption curves for all samples, also illustrated in Fig. 3(d), correspond to type I microporous structures, indicating that microporosity dominates in these materials. Regarding pore properties, as shown in Table 2, the majority of the pore sizes in the substituted mixed-MOFs are below 2.5 nm (UiO-66-$NH_2$: 2.37 nm, BTC-10: 2.24 nm, IP-10: 2.29 nm, BDC-10: 2.48 nm, BA-10: 2.25 nm). The microporous surface areas obtained from BET analysis indicate that micropores constitute >70 % of the total surface area for all samples. This confirms that the pore structure of the mixed-MOFs, regardless of the specific organic ligand substitution, is predominantly microporous.

### 3.2.2. SEM and zeta-potential results

The surface morphology of the mixed MOFs substituted with different organic ligands was examined using SEM at magnifications of 20,000x and 100,000x. At a magnification of 20,000x, as shown in Fig. 4, BDC-10 exhibited relatively larger particles compared to other adsorbents. In contrast, at a magnification of 100,000x, IP-10, BTC-10, and BA-10 consisted of small, spherical particles with a uniform distribution. SEM analysis revealed that, except for $NH_2$-BDC incorporation, the incorporation of different ligands resulted in a reduction in crystal size and the loss of the original crystal morphology.

Zeta potential measurements were conducted at pH 5, consistent with the pH of the RhB solution used in the adsorption tests. As shown in Fig. S2, UiO-66-$NH_2$, IP-10, BTC-10, and BA-10 showed comparable negative zeta potential values (−23.92 mV, −22.15 mV, −24.53 mV, and −23.31 mV, respectively), while BDC-10 exhibited a slightly more negative value (−30.03 mV). These results suggest that the introduction of mixed ligands did not significantly alter the surface charge of the MOFs. All materials presenting a negative surface charge, which would be favorable for the adsorption of cationic RhB. However, the comparable surface charges suggest that surface charge is not the primary governing factor. Instead, variations in pore structure, such as surface area and specific chemical interactions, appear to play a more decisive role in determining adsorption efficiency.

### 3.2.3. $H^1$-NMR results

To confirm the co-integration of linkers, $^1$H—NMR spectroscopy was performed on digested samples of the parent UiO-66-$NH_2$ and the mixed-ligand MOFs (BA-10, BTC-10, BDC-10, and IP-10 using 1 M NaOH in $D_2O$. The resulting $^1$H—NMR spectrum of the digested parent UiO-66-$NH_2$ (Fig. S3(a)) displayed the characteristic peaks of the $NH_2$-BDC linker [49]. Notably, the spectra of all digested mixed-ligand MOFs (BA-10: Fig. S3(b) and Fig. S4; BTC-10: Fig. S3(c); BDC-10: Fig S3(d); and IP-10: Fig 5) exhibited distinct signals corresponding to both the original $NH_2$-BDC linker and the respective secondary linkers (BA, BTC, BDC, or IP) [49,69-71]. The concurrent observation of signals from both linker types provides strong evidence for their successful incorporation within the same MOF framework.

**Table 2**
Summary of BET surface area, micropore ratio, and pore diameter of the synthesized UiO-66-$NH_2$ with the 10 mol % substitutions of different organic ligands, including BTC-10, BDC-10, IP-10, BA-10, and the pristine.

| Adsorbent | Surface area ($m^2/g$) | | | Micropore ratio ( %) | Pore diameter (nm) |
|---|---|---|---|---|---|
| | Total | Micropore | Mesopore | | |
| UiO-66-$NH_2$ | 791.47 | 628.98 | 162.49 | 79.5 | 2.37 |
| BTC-10 | 1161.65 | 838.70 | 322.95 | 72.3 | 2.24 |
| IP-10 | 1331.87 | 990.74 | 341.13 | 74.4 | 2.29 |
| BDC-10 | 909.82 | 688.00 | 221.82 | 75.6 | 2.48 |
| BA-10 | 866.04 | 655.86 | 210.18 | 75.7 | 2.25 |

### 3.3. Adsorption efficiency comparison

The adsorption tests of the mixed-MOFs substituted with different organic ligands were conducted. As shown in Fig. 6(a), the unmodified UiO-66-$NH_2$ exhibited limited adsorption capacity for RhB. It is primarily attributed to its relatively small specific surface area, which restricts the ability of the pollutant to effectively penetrate the adsorbent's pores for removal. Although the presence of -$NH_2$ groups could potentially assist adsorption through hydrogen bonding, the overall removal efficiency of RhB by UiO-66-$NH_2$ remained insufficient.

The BTC-10 sample showed a significant increase in specific surface area. However, its removal efficiency of RhB remained suboptimal. This inefficiency can likely be attributed to the relatively large molecular size of RhB (14.4 × 10.9 × 6.4 Å) [72], which may cause steric hindrance when interacting with the $H_3$BTC-modified pores. The size mismatch between the RhB molecules and the pores prevents effective penetration of the dye into the internal structure of the adsorbent, thus reducing the overall adsorption efficiency. Additionally, the complex molecular structure of $H_3$BTC, which contains two free carboxylate groups, might contribute to the blockage of internal active sites within the adsorbent. These carboxylate groups could potentially shield the active sites, hindering effective contact between the adsorbent and the pollutant, further compromising the material's ability to remove RhB effectively.

In the case of the BA-10 sample, although the TML strategy resulted in larger defects, the absence of free carboxylate groups, which could act as hydrogen bond acceptors, limited its ability to form hydrogen bonds with RhB, a hydrogen bond donor. This lack of supplementary adsorption mechanisms likely contributed to the poor adsorption performance. The BDC-10 sample exhibited larger pores and a greater specific surface area compared to UiO-66-$NH_2$. This increase in surface area and pore size contributed to an improvement in RhB removal efficiency, as the larger pores more easily accommodated the RhB molecules. Finally, the IP-10 sample achieved the best RhB removal performance. This can be attributed to its combination of the highest specific surface area (1331.87 $m^2/g$) among the synthesized samples and the presence of a single free carboxylate group, which facilitated hydrogen bond-assisted adsorption. The relationship between total specific surface area, pore size, and removal efficiency is depicted in Fig. 6(b) and (c), highlighting the superior performance of IP-10.

To ensure reproducibility, IP-10 was re-synthesized, and RhB adsorption tests were repeated in triplicate. As shown in Fig. S5 and Table S2, the experimental $q_e$ values (27.19, 28.10, and 27.90 mg/g) demonstrated excellent consistency, confirming the reliability of the results. To evaluate reusability, the spent IP-10 was regenerated by washing with 1 M HCl, followed by deionized water. Although the dye color visibly faded, complete RhB desorption remained difficult, as shown in Fig. S6. In Fig. S7, XRD analysis confirmed the preservation of the crystalline structure after adsorption and acidic treatment. The initial RhB removal efficiency was 92.43 %, which decreased to 53.67 % and 50.46 % after the first and second regeneration cycles, respectively, as shown in Fig. S8. The decline is attributed to strong dye-framework interactions that hinder full regeneration. Nevertheless, the minimal drop between cycles suggests stable adsorption capacity, and with further optimization of regeneration protocols, IP-10 remains a promising candidate for practical wastewater treatment applications.

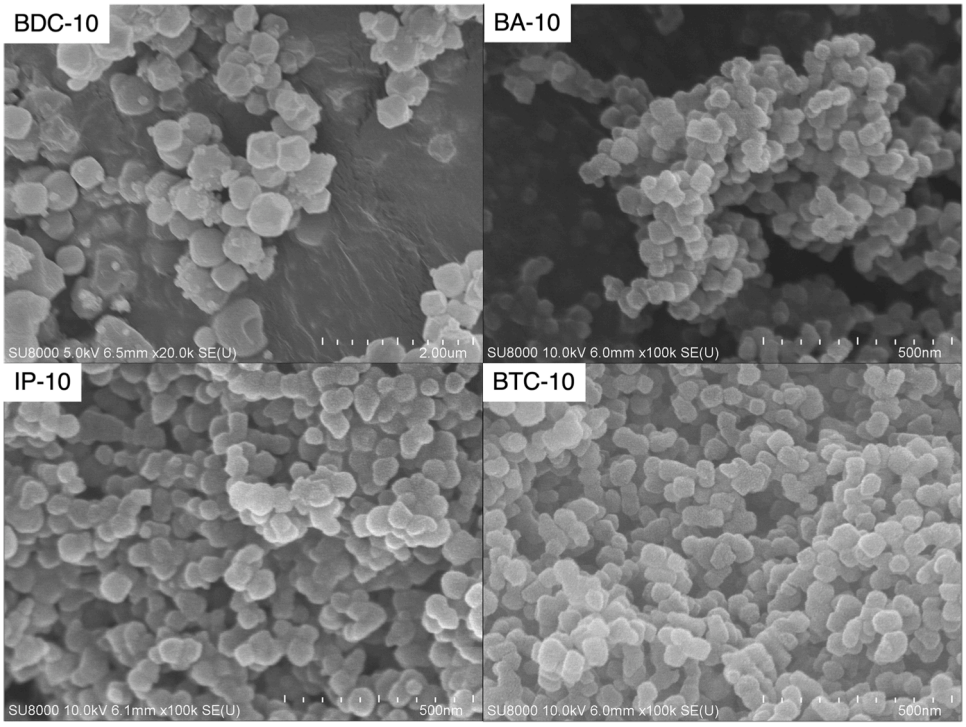


**Fig. 4.** SEM images of the synthesized UiO-66-$NH_2$ with the 10 mol % substitutions of different organic ligands, including BTC-10, BDC-10, IP-10, and BA-10.

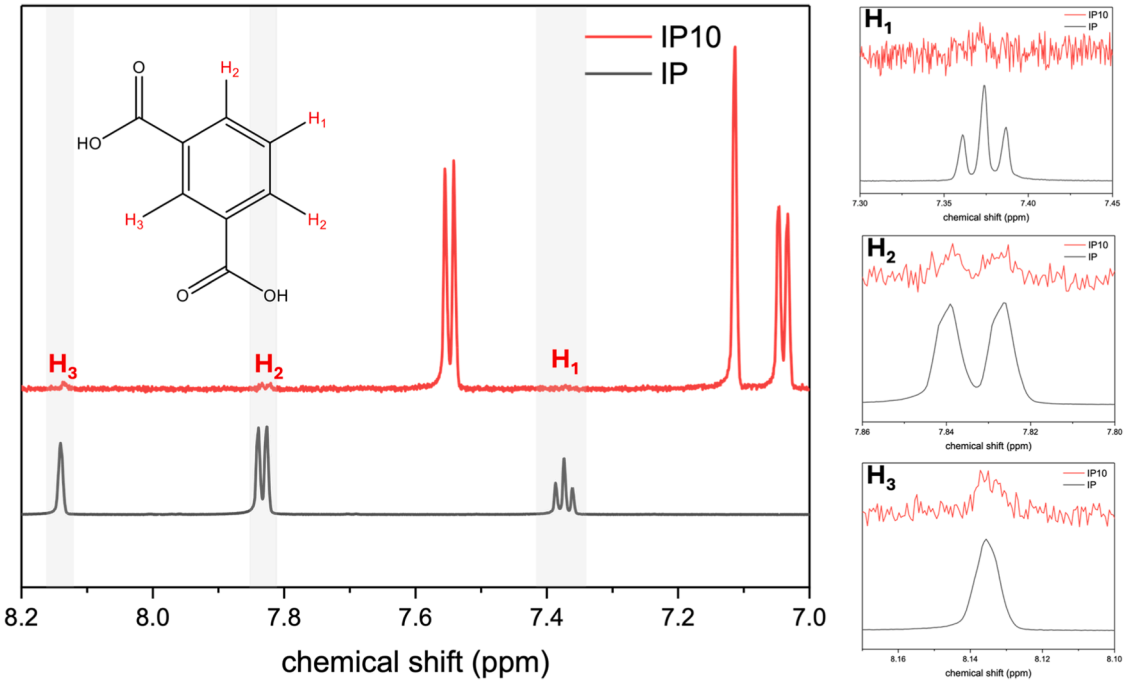


**Fig. 5.** Detailed $H^1$-NMR spectrum of IP-10.

Moreover, to further assess dye removal versatility, additional adsorption experiments were conducted using anionic methyl orange (MO) on both UiO-66-$NH_2$ and IP-10. As shown in Fig. S9, IP-10 achieved a higher MO removal efficiency (91.61 %) compared to UiO-66-$NH_2$ (87.51 %). This improvement highlights the broader applicability of the mixed-ligand strategy, with the enhanced structure and porosity of IP-10 contributing to effective adsorption of both cationic and anionic dyes.

### *3.4. Kinetic analysis of mixed-MOFs with different organic ligand substitutions*

The adsorption kinetics of RhB were investigated by observing its uptake at different contact times on the various mixed-MOFs and fitting the data to both pseudo-first-order and pseudo-second-order kinetic models, as shown in Fig. 7(a) and (b), respectively. The corresponding kinetic parameters are summarized in Tables 3 and 4. As shown in Table 3, the pseudo-first-order model produced poor correlation

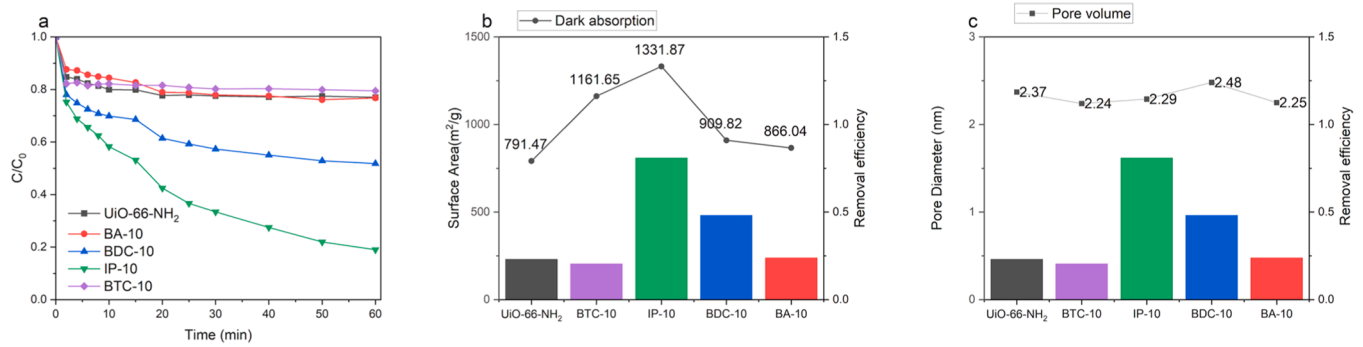


**Fig. 6.** (a) RhB removal efficiency, (b) relationship between RhB removal efficiency and total specific surface area, and (c) relationship between RhB removal efficiency and pore size of the synthesized UiO-66-$NH_2$ with the 10 mol % substitutions of different organic ligands, including BTC-10, BDC-10, IP-10, BA-10, and the pristine.

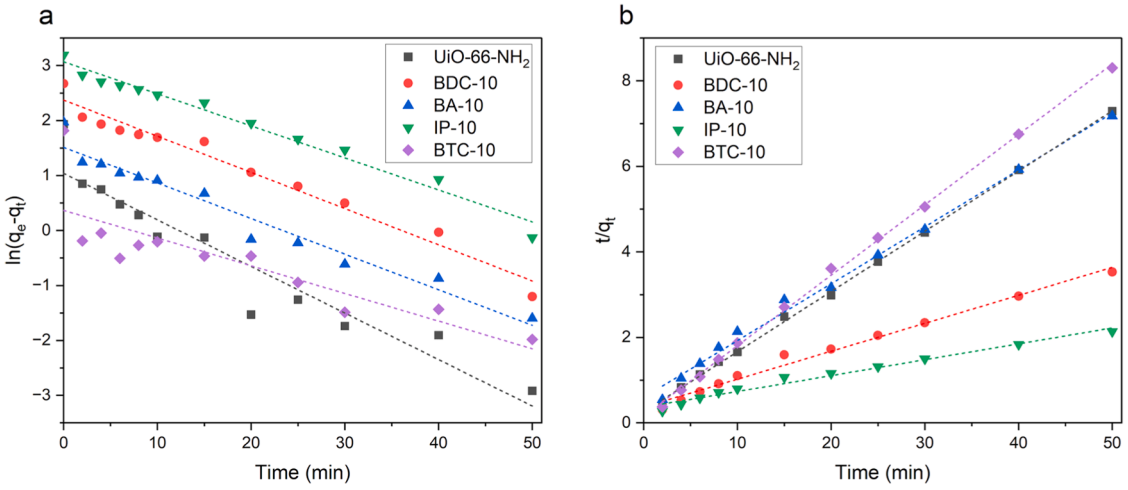


**Fig. 7.** (a) Linear fit of the pseudo-first-order kinetic model and (b) Linear fit of the pseudo-second-order kinetic model for RhB removal efficiency over the synthesized UiO-66-$NH_2$ with the 10 mol % substitutions of different organic ligands, including BTC-10, BDC-10, IP-10, BA-10, and the pristine.

**Table 3**
Kinetic analysis using the pseudo-first-order adsorption kinetic model.

| Adsorbent | $k_1$ ($min^{-1}$) | $q_e$ ($mg \cdot g^{-1}$) | | $R^2$ |
|---|---|---|---|---|
| | | Exp. | Cal. | |
| UiO-66-$NH_2$ | 0.0760 | 6.91 | 2.83 | 0.8315 |
| BTC-10 | 0.1314 | 6.16 | 1.02 | 0.9118 |
| IP-10 | 0.0034 | 24.29 | 21.51 | 0.9763 |
| BA-10 | 0.0277 | 7.17 | 4.54 | 0.9736 |
| BDC-10 | 0.0106 | 14.45 | 10.73 | 0.9728 |

**Table 4**
Kinetic analysis using the pseudo-second-order adsorption kinetic model.

| Adsorbent | $k_2$ ($g \cdot mg^{-1} \cdot min^{-1}$) | $q_e$ ($mg \cdot g^{-1}$) | | $R^2$ |
|---|---|---|---|---|
| | | Exp. | Cal. | |
| UiO-66-$NH_2$ | 0.0760 | 6.91 | 7.11 | 0.9995 |
| BTC-10 | 0.1314 | 6.16 | 6.18 | 0.9988 |
| IP-10 | 0.0034 | 24.29 | 27.78 | 0.9843 |
| BA-10 | 0.0277 | 7.17 | 7.63 | 0.9958 |
| BDC-10 | 0.0106 | 14.45 | 15.60 | 0.9913 |

coefficients ($R^2$ values). Moreover, the calculated equilibrium adsorption capacity ($q_{e\ cal.}$) derived from the model deviated significantly from the experimental values ($q_{e\ exp.}$), further suggesting that this model does not adequately describe the adsorption mechanism.

In contrast, the pseudo-second-order model provided a much better fit, as evidenced by higher $R^2$ values and a strong agreement between $q_{e\ cal.}$ and $q_{e\ exp.}$, as shown in Table 4. The improved correlation and predictive accuracy imply that chemisorption is the dominant mechanism governing RhB adsorption across the different MOF compositions. The adsorption process likely involves chemical interactions, such as hydrogen bonding between functional groups on the RhB molecules and active sites within the MOF structures. Specifically, hydrogen bond donors on RhB may interact with hydrogen bond acceptors introduced through mixed-ligand substitution, enhancing adsorption capacity [73, 74]. These results underscore the role of ligand functionalization in promoting chemisorptive interactions and affirm the suitability of the pseudo-second-order model for describing the adsorption kinetics of RhB on mixed-ligand MOFs.

To further investigate the pore diffusion effects of RhB adsorption on the mixed-MOFs substituted with different organic ligands, the Weber-Morris model was applied. The relationship between the adsorption capacity $q_t$ and the square root of time $t^{0.5}$ was plotted for each mixed-MOF, as depicted in Fig. 8. Interestingly, the plot revealed multiple linear regions, indicating that the adsorption process involves three distinct steps: (1) First, with a steeper slope, corresponds to the rapid diffusion of RhB molecules from the solution to the external surface of the mixed-MOFs. (2) Second, the adsorption stage, where intraparticle diffusion becomes the rate-determining step. (3) Third, with a much smaller slope, represents the equilibrium stage, where the diffusion rate slows down due to the significantly reduced concentration of RhB in the solution. It suggests that the adsorption rate is influenced by several

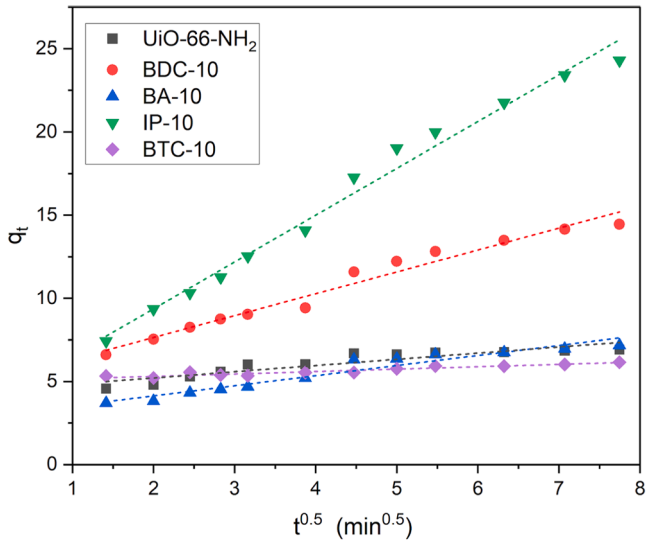


**Fig. 8.** Linear fit of the intraparticle diffusion model for RhB removal efficiency over the synthesized UiO-66-$NH_2$ with the 10 mol % substitutions of different organic ligands, including BTC-10, BDC-10, IP-10, BA-10, and the pristine.

factors, including the size of the pollutant molecules, the pore size distribution of the adsorbent, the concentration of the pollutant, the affinity between the pollutant and the adsorbent, and the diffusion coefficient of the pollutant in the liquid phase.

From the slope of the trendlines, the intraparticle diffusion coefficient ($k_i$) was calculated for all samples and is summarized in Table 5. Among the samples, IP-10 exhibited the highest $R^2$ values (0.9856) in the Weber-Morris model, indicating the best fit. Additionally, IP-10 also had the highest intraparticle diffusion rate constant ($k_i$), reaching 2.8133 $mg.g^{-1}.min^{0.5}$. The high ($k_i$) value for IP-10 indicates that its pore structure is particularly conducive to facilitating rapid intraparticle diffusion, which likely contributes to its superior adsorption performance for RhB. The multi-step adsorption process further highlights the complexity of the adsorption mechanism, where both external diffusion and intraparticle diffusion play significant roles.

## 4. Conclusion

In this study, defect-engineered mixed-ligand Zr-MOFs were successfully synthesized via solvothermal methods by partially substituting $NH_2$-BDC in UiO-66-$NH_2$ with various organic linkers. Initial screening identified 10 mol % $H_3$BTC substitution as optimal, offering improved crystallinity and the highest BET surface area. Building on this, three defect design strategies (IML, HML, and TML) were employed using $H_2$BDC, IP, $H_3$BTC, and BA as co-linkers, yielding four mixed-MOFs (BDC-10, IP-10, BTC-10, and BA-10). BET analysis confirmed that all mixed-MOFs retained predominantly microporous structures, with ligand substitution influencing surface area and functionality. Among them, IP-10 exhibited the highest surface area (1331.87 $m^2/g$) and RhB adsorption capacity (24.29 mg/g), attributed to its single free carboxylate group promoting hydrogen-bond-assisted adsorption. Kinetic studies showed pseudo-second-order behavior across all samples, indicating chemisorption as the dominant mechanism. Additionally, the Weber–Morris model confirmed pore diffusion as the rate-limiting step, with IP-10 displaying the highest intraparticle diffusion coefficient ($k_i$ = 2.8133 $mg{\cdot}g^{-1}{\cdot}min^{-1}$). The findings demonstrate that strategic ligand substitution in mixed-MOFs can effectively enhance both structural properties and adsorption performance. It offers a promising pathway for designing advanced MOFs for environmental remediation and related applications.

**Table 5**
Kinetic analysis of the intraparticle diffusion model.

| Adsorbent | $k_i$ ($g{\cdot}mg^{-1}{\cdot}min^{-0.5}$) | $R^2$ |
|---|---|---|
| UiO-66-$NH_2$ | 0.3723 | 0.8394 |
| BTC-10 | 0.1432 | 0.8949 |
| IP-10 | 2.8133 | 0.9856 |
| BA-10 | 0.6074 | 0.9345 |
| BDC-10 | 1.314 | 0.9709 |

## CRediT authorship contribution statement

**Duo-Syuan Lin:** Writing – original draft, Formal analysis, Data curation, Conceptualization. **Jun-Han Lin:** Investigation, Formal analysis, Data curation. **To-Yu Wang:** Formal analysis. **Ming-Wei Chen:** Formal analysis, Data curation. **Li-Heng Kao:** Methodology, Investigation. **Wei-Yu Chen:** Investigation. **Kanit Manatura:** Conceptualization. **Hongta Yang:** Investigation. **Van-Huy Nguyen:** Conceptualization. **Chao-Wei Huang:** Writing – review & editing, Writing – original draft, Supervision.

## Declaration of competing interest

The authors declare that they have no known competing financial interests or personal relationships that could have appeared to influence the work reported in this paper.

## Acknowledgments

The authors sincerely thank the National Science and Technology Council (NSTC) in Taiwan for funding under NSTC 113–2221-E-006 −021 -MY3. Special thanks to Prof. Chung-Wei Kung (Department of Chemical Engineering, National Cheng Kung University) for supporting the resources of instruments. The authors also thank the Core Facility Center, National Cheng Kung University, Taiwan, from NSTC 113–2740-M-006–002.

## Supplementary materials

Supplementary material associated with this article can be found, in the online version, at doi:10.1016/j.jtice.2025.106246.

## References

[1] Thiry M.C.J.A.R. Staying alive: Making textiles sustainable. 2011;11:26–32.
[2] Desore A., Narula S.A.J.E., Development, Sustainability. An overview on corporate response towards sustainability issues in textile industry. 2018;20(4):1439–59.
[3] Skjolding LM, Jørgensen Lv, Dyhr KS, Köppl CJ, McKnight US, Bauer-Gottwein P, et al. Assessing the aquatic toxicity and environmental safety of tracer compounds Rhodamine B and Rhodamine WT. Water Res 2021;197. https://doi.org/10.1016/j.watres.2021117109. /06/01.
[4] Priya PS, Nandhini PP, Vaishnavi S, Pavithra V, Almutairi MH, Almutairi BO, et al. Rhodamine B, an organic environmental pollutant induces reproductive toxicity in parental and teratogenicity in F1 generation in vivo. Comparative Biochemistry and Physiology Part C: Toxicology & Pharmacology 2024;280. https://doi.org/10.1016/j.cbpc.2024.109898. /06/01.
[5] Jain R., Mathur M., Sikarwar S., Mittal A.J.Joem. Removal of the hazardous dye rhodamine B through photocatalytic and adsorption treatments. 2007;85(4):956–64.
[6] Hsiao WC, Tseng CH, Huang CW. A facile reflux method to produce ternary CQDs/P25/NH2−MIL-125 for photocatalytic degradation of methylene blue under simulated solar light. J Taiwan Inst Chem Eng 2024;154. https://doi.org/10.1016/j.jtice.2023.105286. /01/01.
[7] Pereira V.R., Isloor A.M., Bhat U.K., Ismail A., Obaid A., Fun H-KJRa. Preparation and performance studies of polysulfone-sulfated nano-titania (S-TiO 2) nanofiltration membranes for dye removal. 2015;5(66):53874–85.
[8] Kumarasamy G, Nachimuthu P, Kumarasamy G, Nachimuthu P. Biodegradable glucose and glucosamine grafted polyacrylamide/graphite composites for the removal of acid violet 17 from an aqueous solution. e-Polymers 2018;18(4). https://doi.org/10.1515/epoly-2017-0187. -07-01.
[9] Jiang S, Xu L, Lyu Y, Zhang J, Wu F, Zhang X, et al. Adsorption mechanism of Rhodamine wastewater in the MOFs materials: Effect of metal center and organic

ligand. Sep Purif Technol 2025;363. https://doi.org/10.1016/j.seppur.2025.132056. /08/14.
[10] Kumar K.Y., Muralidhara H., Nayaka Y.A., Balasubramanyam J., Hanumanthappa HJPt. Low-cost synthesis of metal oxide nanoparticles and their application in adsorption of commercial dye and heavy metal ion in aqueous solution. 2013;246:125–36.
[11] Tan Y.X., He Y.P., Wang M., Zhang JJRa. A water-stable zeolite-like metal–organic framework for selective separation of organic dyes. 2014;4(3):1480–3.
[12] Jiang S, Xu L, Lyu Y, Zhang J, Wu F, Zhang X, et al. Adsorption mechanism of Rhodamine wastewater in the MOFs materials: Effect of metal center and organic ligand. Sep Purif Technol 2025:132056.
[13] Su W, Xiang Y, Dai Y, Wang Y, Zhong S, Li J. Challenges and recent advances in MOF-based gas separation membranes. Chemical Communications 2024.
[14] Khafaga DS, El-Morsy MT, Faried H, Diab AH, Shehab S, Saleh AM, et al. Metal–organic frameworks in drug delivery: engineering versatile platforms for therapeutic applications. RSC Adv 2024;14(41):30201–29.
[15] Fisher TM, dos Santos AJ, Garcia-Segura S. Recent Advances and Prospective Challenges of Iron Metal–Organic Framework (MOF) Catalysts in Electrochemical Fenton Treatment Technologies. Curr Pollut Rep 2025;11(1):1–18.
[16] Gautam S., Agrawal H., Thakur M., Akbari A., Sharda H., Kaur R., et al. Metal oxides and metal organic frameworks for the photocatalytic degradation: a review. 2020;8(3):103726.
[17] Hsiao WC, Tseng CH, Huang CW. A facile reflux method to produce ternary CQDs/P25/NH2−MIL-125 for photocatalytic degradation of methylene blue under simulated solar light. J Taiwan Inst Chem Eng 2023:105286. https://doi.org/10.1016/j.jtice.2023.105286.
[18] Molavi H., Zamani M., Aghajanzadeh M., Kheiri Manjili H., Danafar H., Shojaei A. J.A.O.C. Evaluation of UiO-66 metal organic framework as an effective sorbent for Curcumin's overdose. 2018;32(4):e4221.
[19] Liu C.S., Zhang Z.H., Chen M., Zhao H., Duan F.H., Chen D-M, et al. Pore modulation of zirconium–organic frameworks for high-efficiency detection of trace proteins. 2017;53(28):3941–4.
[20] Teo H.W.B., Chakraborty A., Kayal S.J.M., Materials M. Formic acid modulated (fam) aluminium fumarate MOF for improved isotherms and kinetics with water adsorption: Cooling/heat pump applications. 2018;272:109–16.
[21] Ren Q., Nie M., Yang L., Wei F., Ding B., Chen H., et al. Synthesis of MOFs for RhB Adsorption from Wastewater. 2022;10(3):27.
[22] Cui W, Kang X, Zhang X, Cui X. Gel-like ZnO/Zr-MOF(bpy) nanocomposite for highly efficient adsorption of Rhodamine B dye from aqueous solution. Journal of Physics and Chemistry of Solids 2019;134. https://doi.org/10.1016/j.jpcs.2019.06.004. /11/01.
[23] Ibrahim AA, Kaid MM, Ali SL, Samra SE, El-Hakam SA, Ahmed AI. Applications of nanostructure phosphomolybdic acid/strontium MOF for removal of Rhodamine B and synthesis of pharmaceutically significant 14-Aryl-14-alkyl-14-H-dibenzoxanthene and 7-hydroxy-4-methyl coumarin. Inorg Chem Commun 2023;153. https://doi.org/10.1016/j.inoche.2023.110748. /07/01.
[24] Patil SS, Behare KP, Sonawane GH, Labhane PK. The amalgamated impact of bimetals, amino groups, and cross-linked structures of MOF on MOF for the removal of cationic dyes. Inorg Chem Commun 2024;170. https://doi.org/10.1016/j.inoche.2024.113246. /12/01.
[25] Schaate A., Roy P., Godt A., Lippke J., Waltz F., Wiebcke M., et al. Modulated synthesis of Zr-based metal–organic frameworks: from nano to single crystals. 2011;17(24):6643–51.
[26] Cavka J.H., Jakobsen S., Olsbye U., Guillou N., Lamberti C., Bordiga S., et al. A new zirconium inorganic building brick forming metal organic frameworks with exceptional stability. 2008;130(42):13850–1.
[27] Feng D., Gu Z.Y., Li J.R., Jiang H.L., Wei Z., Zhou HCJACIE. Zirconium-metalloporphyrin PCN-222: mesoporous metal–organic frameworks with ultrahigh stability as biomimetic catalysts. 2012;51(41):10307–10.
[28] Burtch N.C., Jasuja H., Walton KSJCr. Water stability and adsorption in metal–organic frameworks. 2014;114(20):10575–612.
[29] Wu H., Yildirim T., Zhou WJTjopcl. Exceptional mechanical stability of highly porous zirconium metal–organic framework UiO-66 and its important implications. 2013;4(6):925–30.
[30] Zhang M., Chen Y.P., Bosch M., Gentle III T., Wang K., Feng D., et al. Symmetry-guided synthesis of highly porous metal–organic frameworks with fluorite topology. 2014;126(3):834–7.
[31] Kandiah M., Nilsen M.H., Usseglio S., Jakobsen S., Olsbye U., Tilset M., et al. Synthesis and stability of tagged UiO-66 Zr-MOFs. 2010;22(24):6632–40.
[32] Kim S., Lee J., Son Y., Yoon MJBotKCS. Study of the Dye Adsorption Kinetics of Metal–Organic Frameworks in Aqueous Media. 2020;41(8):843–50.
[33] Garibay S.J., Cohen SMJCc. Isoreticular synthesis and modification of frameworks with the UiO-66 topology. 2010;46(41):7700–2.
[34] Taddei MJCCR. When defects turn into virtues: The curious case of zirconium-based metal-organic frameworks. 2017;343:1–24.
[35] Valenzano L., Civalleri B., Chavan S., Bordiga S., Nilsen M.H., Jakobsen S., et al. Disclosing the complex structure of UiO-66 metal organic framework: a synergic combination of experiment and theory. 2011;23(7):1700–18.
[36] Wu H., Chua Y.S., Krungleviciute V., Tyagi M., Chen P., Yildirim T., et al. Unusual and highly tunable missing-linker defects in zirconium metal–organic framework UiO-66 and their important effects on gas adsorption. 2013;135(28):10525–32.
[37] Shearer G.C., Chavan S., Bordiga S., Svelle S., Olsbye U., Lillerud KPJCoM. Defect engineering: tuning the porosity and composition of the metal–organic framework UiO-66 via modulated synthesis. 2016;28(11):3749–61.
[38] Jiang J., Gándara F., Zhang Y.B., Na K., Yaghi O.M., Klemperer WGJJotACS. Superacidity in sulfated metal–organic framework-808. 2014;136(37):12844–7.
[39] Ou R., Zhu W., Li L., Wang X., Wang Q., Gao Q., et al. Boosted capture of volatile organic compounds in adsorption capacity and selectivity by rationally exploiting defect-engineering of UiO-66 (Zr). 2021;266:118087.
[40] Annadurai G., Juang R.S., Lee D-JJJohm. Use of cellulose-based wastes for adsorption of dyes from aqueous solutions. 2002;92(3):263–74.
[41] Schaate A, Roy P, Godt A, Lippke J, Waltz F, Wiebcke M, et al. Modulated synthesis of Zr-based metal–organic frameworks: from nano to single crystals. Chemistry–A European Journal 2011;17(24):6643–51.
[42] Ren J., Langmi H.W., North B.C., Mathe M., Bessarabov DJijohe. Modulated synthesis of zirconium-metal organic framework (Zr-MOF) for hydrogen storage applications. 2014;39(2):890–5.
[43] Gu Y.M., Yuan Y.Y., Qadir S., Yuan Z.S., Zhao S.S., Sun T.J., et al. Mixed-Linker Metal-Organic frameworks for carbon and hydrocarbons capture under moist conditions. 2022;433:134447.
[44] Chun H., Dybtsev D.N., Kim H., Kim KJCAEJ. Synthesis, X-ray crystal structures, and gas sorption properties of pillared square grid nets based on paddle-wheel motifs: Implications for hydrogen storage in porous materials. 2005;11(12):3521–9.
[45] Chen W., Wang J.Y., Chen C., Yue Q., Yuan H.M., Chen J.S., et al. Photoluminescent metal− organic polymer constructed from trimetallic clusters and mixed carboxylates. 2003;42(4):944–6.
[46] Bunck D.N., Dichtel WRJCAEJ. Mixed linker strategies for organic framework functionalization. 2013;19(3):818–27.
[47] Chakrabarty R., Mukherjee P.S., Stang PJJCr. Supramolecular coordination: self-assembly of finite two-and three-dimensional ensembles. 2011;111(11):6810–918.
[48] Chen J, Guo T, Gao H, He T, Li J, Li H, et al. Eu3+-Doped Mixed-Ligand UiO-66-Type Metal–Organic Framework for Ratiometric Fluorescence Sensing Fluoride Ions with Ultralow Detection Limit. ACS Applied Materials & Interfaces October 25 2024;16(44). https://doi.org/10.1021/acsami.4c13284.
[49] Vo TK, Le VN, Nguyen VC, Song M, Kim D, Yoo KS, et al. Microwave-assisted continuous-flow synthesis of mixed-ligand UiO-66(Zr) frameworks and their application to toluene adsorption. Journal of Industrial and Engineering Chemistry 2020;86. https://doi.org/10.1016/j.jiec.2020.03.001. /06/25.
[50] Kalaj M, Kalaj M, Palomba JM, Palomba JM, Bentz KC, Bentz KC, et al. Multiple functional groups in UiO-66 improve chemical warfare agent simulant degradation. Chemical Communications 2019;55(37). https://doi.org/10.1039/C9CC02252J. /05/02.
[51] Tsuruoka T., Furukawa S., Takashima Y., Yoshida K., Isoda S., Kitagawa S.J.A.C. Nanoporous nanorods fabricated by coordination modulation and oriented attachment growth. 2009;121(26):4833–7.
[52] Barylak M, Cendrowski K, Mijowska E. Application of Carbonized Metal–Organic Framework as Efficient Adsorbent of Cationic Dye. Ind Eng Chem Res 2018;57(14). https://doi.org/10.1021/acs.iecr.7b03790. March 21.
[53] Majumdar P., Khan A.Y., Bandyopadhyaya RJBEJ. Diffusion, adsorption and reaction of glucose in glucose oxidase enzyme immobilized mesoporous silica (SBA-15) particles: experiments and modeling. 2016;105:489–96.
[54] Baraka AJJoECE. Investigation of temperature effect on surface-interaction and diffusion of aqueous-solution/porous-solid adsorption systems using diffusion–binding model. 2015;3(1):129–39.
[55] Nanthamathee C., Chantarangkul C., Jakkrawhad C., Payaka A., Dechatiwongse P. J.H. Fine-tuning the dye adsorption capacity of UiO-66 by a mixed-ligand approach. 2022;8(2):e08961.
[56] Jamshidifard S., Koushkbaghi S., Hosseini S., Rezaei S., Karamipour A., Irani MJJohm. Incorporation of UiO-66-NH2 MOF into the PAN/chitosan nanofibers for adsorption and membrane filtration of Pb (II), Cd (II) and Cr (VI) ions from aqueous solutions. 2019;368:10–20.
[57] Behvandi A., Safekordi A., Khorasheh FJJoPM. Removal of benzoic acid from industrial wastewater using metal organic frameworks: equilibrium, kinetic and thermodynamic study. 2017;24(1):165–78.
[58] Azizian SJJoc, Science I. Kinetic models of sorption: a theoretical analysis. 2004;276(1):47–52.
[59] Ho Y-SJJohm. Review of second-order models for adsorption systems. 2006;136(3):681–9.
[60] Weber Jr W.J., Morris JCJJotsed. Kinetics of adsorption on carbon from solution. 1963;89(2):31–59.
[61] Banerjee D, Xu W, Nie Z, Johnson LEV, Coghlan C, Sushko ML, et al. Zirconium-Based Metal–Organic Framework for Removal of Perrhenate from Water. Inorg Chem 2016;55(17):8241–3. https://doi.org/10.1021/acs.inorgchem.6b01004.
[62] Drout R.J., Howarth A.J., Otake K-i, Islamoglu T., Farha O.K.J.C. Efficient extraction of inorganic selenium from water by a Zr metal–organic framework: investigation of volumetric uptake capacity and binding motifs. 2018;20(40):6140–5.
[63] Pangestu A., Lestari W.W., Wibowo F.R., Larasati LJJoI, Polymers O, Materials. Green Electro-Synthesized MIL-101 (Fe) and Its Aspirin Detoxification Performance Compared to MOF-808. 2022;32(5):1828–39.
[64] Ibrahim M., Nada A., Kamal D.E. Density functional theory and FTIR spectroscopic study of carboxyl group. 2005.
[65] Sonibare OO, Haeger T, Foley SFJE. Structural characterization of Nigerian coals by X-ray diffraction. Raman and FTIR spectroscopy 2010;35(12):5347–53.
[66] Nguyen K.D., Ho P.H., Vu P.D., Pham T.L., Trens P., Di Renzo F., et al. Efficient Removal of Chromium (VI) Anionic Species and Dye Anions from Water Using MOF-808 Materials Synthesized with the Assistance of Formic Acid. 2021;11(6):1398.
[67] Van Tam T., Hur S.H., Chung J.S., Choi W.M.J.S., Chemical A.B. Novel paper-and fiber optic-based fluorescent sensor for glucose detection using aniline-functionalized graphene quantum dots. 2021;329:129250.

[68] Zhao Y., Wang D., Wei W., Cui L., Cho C.W., Wu G.J.E.S., et al. Effective adsorption of mercury by Zr (IV)-based metal-organic frameworks of UiO-66-NH2 from aqueous solution. 2021;28(6):7068–75.
[69] Sannes DK, Øien-Ødegaard S, Aunan E, Nova A, Olsbye U. Quantification of Linker Defects in UiO-Type Metal–Organic Frameworks. Chemistry of Materials 2023;35 (10). https://doi.org/10.1021/acs.chemmater.2c03744. May 8.
[70] Zhou C, Li H, Qin H, Yuan B, Zhang M, Wang L, et al. Defective UiO-66-NH2 monoliths for optimizing CO2 capture performance. Chemical Engineering Journal 2023;467. https://doi.org/10.1016/j.cej.2023.143394. /07/01.
[71] Nguyen KD, Vo NT, Le KTM, Ho KV, Phan NTS, Ho PH, et al. Defect-engineered metal–organic frameworks (MOF-808) towards the improved adsorptive removal of organic dyes and chromium (vi) species from water. New Journal of Chemistry 2023;47(13). https://doi.org/10.1039/D2NJ05693C. /03/27.
[72] Huang J.H., Huang K.L., Liu S.Q., Wang A.T., Yan C.J.C., Physicochemical S.A., et al. Adsorption of Rhodamine B and methyl orange on a hypercrosslinked polymeric adsorbent in aqueous solution. 2008;330(1):55–61.
[73] Song J.Y., Ahmed I., Seo P.W., Jhung SHJAam, interfaces. UiO-66-type metal–organic framework with free carboxylic acid: versatile adsorbents via H-bond for both aqueous and nonaqueous phases. 2016;8(40):27394–402.
[74] Vadivelan V., Kumar KVJJoc, science i. Equilibrium, kinetics, mechanism, and process design for the sorption of methylene blue onto rice husk. 2005;286(1): 90–100.